Rhombohedral Distortion of the Cubic MgCu$_2$-Type Structure in Ca$_2$Pt$_3$Ga and Ca$_2$Pd$_3$Ga

Asa Toombs [1,2] **and Gordon J. Miller** [1,2,*]

1   Department of Chemistry, Iowa State University, Ames, IA 50011-3111, USA; toombsa@iastate.edu
2   Ames Laboratory, U.S. Department of Energy, Ames, IA 50011-3111, USA
*   Correspondence: gmiller@iastate.edu

Abstract: Two new fully ordered ternary Laves phase compounds, Ca$_2$Pt$_3$Ga and Ca$_2$Pd$_3$Ga, have been synthesized and characterized by powder and single-crystal X-ray diffraction along with electronic structure calculations. Ca$_2$Pd$_3$Ga was synthesized as a pure phase whereas Ca$_2$Pt$_3$Ga was found as a diphasic product with Ca$_2$Pt$_2$Ga. Electronic structure calculations were performed to try and understand why CaPt$_2$ and CaPd$_2$, which crystalize in the cubic MgCu$_2$-type Laves phase structure, distort to the ordered rhombohedral variant, first observed in the magneto-restricted TbFe$_2$ compound, with the substitution of twenty-five percent of the Pt/Pd with Ga. Electronic stability was investigated by changing the valence electron count from 22e^-/f.u. in CaPd$_2$ and CaPt$_2$ (2x) to 37e^-/f.u. in Ca$_2$Pd$_3$Ga and Ca$_2$Pt$_3$Ga, which causes the Fermi level to shift to a more energetically favorable location in the DOS. The coloring problem was studied by placing a single Ga atom in each of four tetrahedra of the cubic unit cell of the MgCu$_2$-type structure, with nine symmetrically inequivalent models being investigated. Non-optimized and optimized total energy analyses of structural characteristics, along with electronic properties, will be discussed.

Keywords: coloring problem; band structure; structure optimizations; polar intermetallics; ternary Laves phases; electronic structure; X-ray diffraction; total energy

1. Introduction

Platinum exhibits the second largest relativistic contraction of the 6s orbitals, second only to Au [1], and has interesting catalytic properties, thus making it an interesting metal to study, especially in reduced environments. Exploration of the Ca-Pt-X (X = Ga, In) system revealed a new ternary compound, Ca$_2$Pt$_3$Ga, which turned out to be an ordered rhombohedral distortion of the MgCu$_2$-type Laves phase CaPt$_2$. After Ca$_2$Pt$_3$Ga was synthesized, the Pd analog was targeted and successfully prepared as an isostructural compound.

Laves phases are the largest class of intermetallic compounds with the general formula AB$_2$. Binary Laves phases primarily crystalize in one of three crystal structures: MgCu$_2$, MgZn$_2$, or MgNi$_2$ [2]. These structure types, which appear in a vast number of intermetallic systems, contain topologically closed-packed Frank–Kasper polyhedra and have been intensely studied for magnetic and magnetocaloric properties, hydrogen storage, and catalytic behavior [3–9]. The stability of Laves phases has been described by using geometrical and electronic structure factors. Geometrical factors include packing densities and atomic size ratios of A/B whereas electronic factors include valence electron count (*vec*) and difference in electronegativities between A and B [10,11].

To tune the properties and structures of Laves phases, an addition via substitution of a third element into the structure can be explored. The resulting ternary compounds can have mixing on the A and B sites but retain the parent Laves phase structure or the structures can change into a fully ordered ternary Laves phase that is a variant of the parent structure. The first ordered ternary Laves

phase with the direct rhombohedral distortion of the MgCu$_2$-type, first evidenced in the binary TbFe$_2$ phase, which distorts via magnetostriction, was reported to be Mg$_2$Ni$_3$Si [11,12]. Recently, many examples of this rhombohedral distortion, with varying *vec*, have been reported: RE$_2$Rh$_3$Si (RE = Pr, Er), U$_2$Ru$_3$Si, Ce$_2$Rh$_{3+x}$Si$_{1-x}$, RE$_2$Rh$_3$Ge, Ca$_2$Pd$_3$Ge, Sm$_2$Rh$_3$Ge, U$_2$Ru$_3$Ge, Mg$_2$Ni$_3$Ge [2], Mg$_2$Ni$_3$P, and the heretofore only known gallides RE$_2$Rh$_3$Ga (RE = Y, La-Nd, Sm, Gd-Er).

The maximal *translationengleiche* subgroup of the Fd-3m space group that allows for the ordered 3:1 ratio of M:Ga atoms is R-3m [2,3,11]. Reported herein is the first extensive computational study of the "coloring problem" [13] for this rhombohedral distortion of the cubic cell. Formation energies and electronic structure calculations were performed on the binary and ternary Laves phases CaM$_2$ and Ca$_2$M$_3$Ga (M = Pt, Pd) along with total energy calculations of various "coloring models" with the same composition but different atomic arrangements or "colorings".

2. Materials and Methods

2.1. Electronic Structure Calculations

Electronic structure calculations to obtain DOS and COHP curves for bonding analysis were performed on CaM$_2$ and Ca$_2$M$_3$Ga (M = Pd, Pt) using the Stuttgart Tight-Binding, Linear-Muffin-Tin Orbital program with the Atomic Sphere Approximation (TB-LMTO-ASA) [14]. This approximation uses overlapping Wigner-Seitz (WS) spheres surrounding each atom so that spherical basis functions, i.e., atomic orbital (AO)-like wavefunctions, are used to fill space. The WS sphere radii used for the various atoms are: Ca 3.403–3.509 Å, Pt 2.800–2.844 Å, Pd 2.864–2.865 Å, and Ga 2.800–2.951 Å. The total overlap volume was 6.44% for the cubic Laves phase structures and 7.25% and 7.11%, respectively, for Ca$_2$Pt$_3$Ga and Ca$_2$Pd$_3$Ga. No empty spheres were required to attain 100% space filling of the unit cells. The exchange-correlation potential was treated with the von Barth-Hedin formulation within the local density approximation (LDA) [15]. All relativistic effects except spin-orbit coupling were taken into account using a scalar relativistic approximation [16]. The basis sets included 4s/(4p)/3d for Ca, 6s/6p/5d/(5f) for Pt, 5s/5p/4d/(4f) for Pd, and 4s/4p/(4d) for Ga (down-folded orbitals are shown in parentheses). Reciprocal space integrations were performed using *k*-point meshes of 1313 points for rhombohedral Ca$_2$Pt$_3$Ga and Ca$_2$Pd$_3$Ga and 145 points for cubic CaPt$_2$ and CaPd$_2$ in the corresponding irreducible wedges of the first Brillouin zones.

Structure optimization and total energy calculations were performed using the Vienna ab Initio Simulation Package (VASP) [17,18], which uses projector augmented-wave (PAW) [19] pseudopotentials that were treated with the Perdew–Burke–Ernzerhof generalized gradient approximation (PBE-GGA) [20]. Reciprocal space integrations were accomplished over a 13 × 13 × 13 Monkhorst–Pack *k*-point mesh [21] by the linear tetrahedron method [22] with the energy cutoff for the plane wave calculations set at 500.00 eV.

2.2. Synthesis

All ternary compounds were obtained by melting mixtures of Ca pieces (99.99%, Sigma-Aldrich, St. Louis, MO, USA), Pt spheres (99.98%, Ames Laboratory, Ames, IA, USA) or Pd pieces (99.999%, Ames Laboratory), Ga ingots (99.99%, Alfa Aesar, Haverhill, MA, USA), and, in some cases, including Ag powder (99.9% Alfa Aesar). Samples of total weight ca. 300 mg were weighed out in a N$_2$-filled glovebox with <0.1 ppm moisture and sealed in tantalum tubes by arc-melting under an argon atmosphere. To prevent the tantalum tubes from oxidizing during the heating process, they were enclosed in evacuated silica jackets. The silica ampoules were placed in programmable furnaces and heated at a rate of 150 °C per hour to 1050 °C, held there for 3 h, then cooled at 50 °C per hour to 850 °C and annealed for 5 days. The samples were then cooled at 50 °C per hour to room temperature. Ca$_2$Pt$_3$Ga crystals were obtained from a loading of "Ca$_2$Pt$_3$Ga$_{0.85}$Ag$_{0.15}$", whereas Ca$_2$Pd$_3$Ga crystals were obtained from stoichiometric mixtures of these elements.

2.3. Powder X-ray Diffraction

All samples were characterized by powder X-ray diffraction on a STOE WinXPOW powder diffractometer using Cu $K\alpha$ radiation (λ = 1.540598 Å). Each sample was ground using an agate mortar and pestle and then sifted through a US standard sieve with hole sizes of 150 microns. All powder specimens were fixed on a transparent acetate film using a thin layer of vacuum grease, covered by a second acetate film, placed in a holder and mounted in the X-ray diffractometer. Scattered intensities were recorded using a scintillation detector with a step size of 0.03° in 2Θ using a step scan mode ranging from 0° to 130°. Phase analysis was performed using the program PowderCell [23] by overlaying theoretical powder patterns determined from single crystal X-ray diffraction over the powder patterns determined experimentally.

2.4. Single Crystal X-ray Diffraction

Single crystals were extracted from samples and mounted on the tips of thin glass fibers. Intensity data were collected at room temperature on a Bruker SMART APEX II diffractometer with a CCD area detector, distance set at 6.0 cm, using graphite monochromated Mo $K\alpha$ radiation (λ= 0.71073 Å). The data collection strategies were obtained both by a pre-saved set of runs as well as from an algorithm in the program COSMO in the APEX II software package [24]. Indexing and integration of data were performed with the program SAINT in the APEX II package [24,25]. SADABS was used to apply empirical absorption corrections [24]. Crystal structures were solved by direct methods and refined by full-matrix least squares on F^2 using SHELXL [26]. The final refinements were performed using anisotropic displacement parameters on all atoms. All crystal structure figures were produced using the program Diamond [27].

3. Results

3.1. Phase Analysis

Ca_2Pt_3Ga has been synthesized, but not as a pure phase. Using high temperature reactions, this compound can only be synthesized with the addition of a small quantity of silver in the loaded reaction mixture. Without adding silver the binary cubic Laves phase $CaPt_2$ forms as the major product as well as a small amount of some unidentified phase(s) according to X-ray powder diffraction. At reaction and annealing temperatures, Ga, Ca, and Ag are molten and their respective binary phase diagrams indicate miscibility. As Pt dissolves into the liquid, we hypothesize that the presence of Ag slows the reaction rate between Ca and Pt to form $CaPt_2$ and allows Pt and Ga to achieve sufficient mixing in the liquid before crystallizing into Ca_2Pt_3Ga. However, even when synthesized with the addition of silver and at 1050 °C, Ca_2Pt_3Ga does coexists with Ca_2Pt_2Ga and the binary $CaPt_2$. Figure 1 shows the powder pattern for the sample loaded as "$Ca_2Pt_3Ga_{0.85}Ag_{0.15}$" along with the theoretical patterns for the Ca_2Pt_3Ga and Ca_2Pt_2Ga. Peak fitting analysis performed with Jana [28] can be found in Figure S1 along with relative contributions of the three phases.

Three samples with varying silver content, viz., 2.50, 8.33, and 14.29 mole percent Ag, were examined. According to the XPD patterns (see Figure S3 in Supporting Information), as the silver content increased, the yield of Ca_2Pt_2Ga increased. The outcome was also successfully reproducible for the loading "$Ca_2Pt_3Ga_{0.85}Ag_{0.15}$" (see Figure S4).

On the other hand, Ca_2Pd_3Ga can be prepared without the addition of silver. Since Ag and Pd have similar X-ray scattering factors, using Ag for the synthesis of Ca_2Pd_3Ga would present distinct challenges for subsequent characterization. Fortunately, a stoichiometric loading yielded Ca_2Pd_3Ga essentially as a pure phase product, with two non-indexed peaks at 2θ values of 20.0° and 32.8° most likely coming from a slight impurity of $Ca_3Pd_2Ga_2$ (see Figure 2). Figure S2 shows the Rietveld refinement of Ca_2Pt_3Ga. Both compounds Ca_2Pt_3Ga and Ca_2Pd_3Ga degrade in air after approximately two weeks.
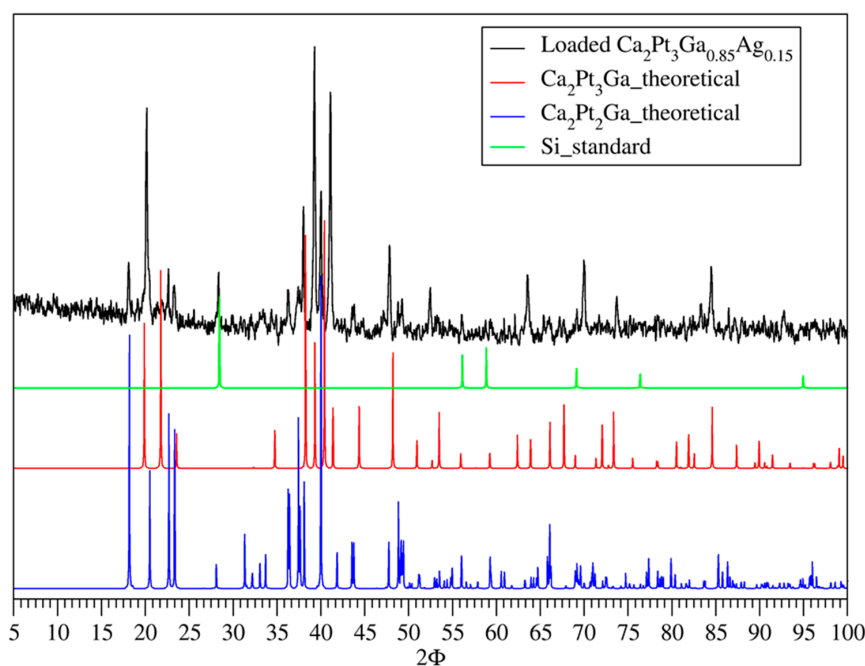
Figure 1. Powder Patterns for Ca_2Pt_3Ga showing the existence of Ca_2Pt_2Ga in the system.
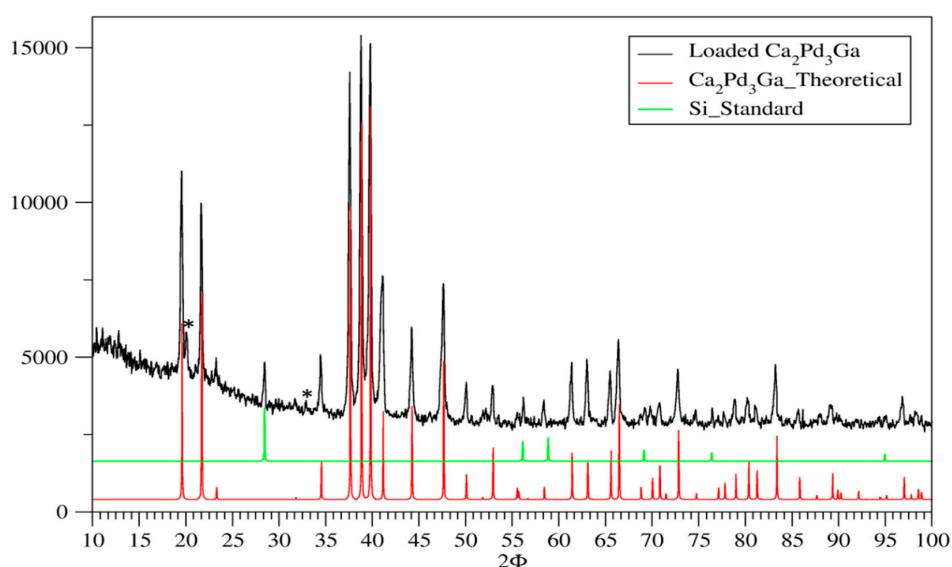
Figure 2. Powder pattern of sample loaded as Ca_2Pd_3Ga. * = non-indexed peaks coming from slight $Ca_3Pd_2Ga_2$ impurity.

3.2. Structure Determination

Several single crystals were selected from the loaded samples and tested on a Bruker SMART APEX II single crystal diffractometer for quality. Among those, the best 3 samples for Ca_2Pt_3Ga and Ca_2Pd_3Ga were examined. The results of single crystal X-ray diffraction on these crystals are found in Table 1 and Table S3. Ca_2M_3Ga (M = Pt, Pd) crystallize in the Y_2Rh_3Ge structure type [29], which is a rhombohedral distortion of the cubic Laves phase $MgCu_2$-type structure, as discussed by Doverbratt et al. [3] and Siggelkow et al. [2]. The M atoms occupy *9e* Wyckoff positions which buildup 3.6.3.6 Kagomé nets orthogonal to the *c*-axis [2]. The Ga atoms cap alternate triangular faces of the Kagomé net and themselves form hexagonal nets. The Ga and M atoms are each coordinated by 6 Ga or M atoms. Nine M and three Ga atoms surround each Ca atom in a slightly distorted Frank-Kasper polyhedral

environment. The rhombohedral structure of Ca_2M_3Ga has no Ga-Ga nearest neighbor interactions, with distances ($6\times/6\times$) of 5.2361(9)/5.576(1) Å and 5.2331(6)/5.6326(8) Å for the Pt and Pd cases, respectively [3]. For the binary compounds CaM_2, each type of nearest neighbor interaction, i.e., Ca-Ca, Ca-M, and M-M, has a single length. When the structure distorts rhombohedrally to incorporate Ga atoms, the Ca-Ca and Ca-M contacts each split into two different distances: there are three shorter and one longer Ca-Ca interactions; whereas six Ca-M interactions that are longer and three shorter. Atomic positions and anisotropic displacement parameters for both compounds can be found in Tables S1 and S2.

Table 1. Crystallographic information for Ca_2Pt_3Ga and Ca_2Pd_3Ga.

Sample	Ca_2Pt_3Ga	Ca_2Pd_3Ga
Space Group	*R-3m*	*R-3m*
Unit Cell Dim.	$a = 5.576(1)$ Å $c = 12.388(3)$ Å	$a = 5.6326(8)$ Å $c = 12.300(2)$ Å
Volume	333.6(2) Å^3	337.9(1) Å^3
Z	3	3
Theta range for data collection	4.530 to 28.922°	4.495 to 49.319°
Index ranges	$-7 \leq h \leq 7, -7 \leq k \leq 7, -16 \leq l \leq 16$	$-11 \leq h \leq 11, -11 \leq k \leq 11, -26 \leq l \leq 26$
Reflections Collected	1321	4878
Independent Reflections	126 [R(int) = 0.0485]	460 [R(int) = 0.0585]
Data/restraints/parameters	126/0/11	460/0/11
Goodness-of-fit	1.078	1.091
Final R indices [I > 2sigma(l)]	R1 = 0.0179, wR2 = 0.0403	R1 = 0.0208, wR2 = 0.0403
R indices (all data)	R1 = 0.0179, wR2 = 0.0403	R1 = 0.0251, wR2 = 0.0414
Extinction Coefficient	0.0008(1)	0.0036(3)
Largest diff. peak and hole	3.366 and -2.052 e·Å^{-3}	1.697 and -2.657 e·Å^{-3}

3.3. Coloring Models and Electronic Structure Calculations

To elucidate the driving force that leads to the rhombohedral arrangement of Pt/Pd and Ga atoms in the majority atom positions of the cubic Laves phase, Burnside's lemma [30] was used to construct nine distinct structural models for the unit cells formulated as $Ca_8[M_3Ga]_4$ [31]. These models are illustrated in Figure S5 along with their respective space groups. The total energy of each model, listed in Table 2, was calculated using VASP without optimization. These results show that the rhombohedral model (α) is the lowest in energy. There are three models that have no nearest neighbor Ga-Ga interactions, these include the rhombohedral coloring, a cubic coloring (μ), and an orthorhombic coloring (γ). The rhombohedral and cubic models are the two lowest in energy before optimization, whereas the orthorhombic coloring is the second highest in energy.

Table 2. Total energy of non-optimized and optimized coloring models showing optimized Ga-Ga distances.

	Ca_2Pt_3Ga				Ca_2Pd_3Ga		
Model	Ga-Ga Distance (Å)	meV Non-Optimized	meV Optimized	# Ga-Ga Interactions	meV Optimized	meV Non-Optimized	Ga-Ga Distance (Å)
Alpha	5.276	0	0	0	0	0	5.282
Beta	2.755	+38.5	+78.8	1	+68.1	+30.5	2.732
Delta	2.811	+62.1	+121.8	2	+121.8	+59.3	2.775
Epsilon	2.808	+50.8	+95.7	1	+73.0	+36.0	2.800
Gamma	4.738	+140.7	+56.0	0	+26.0	+92.0	4.791
Iota	2.931	+70.5	+113.4	2	+104.7	+61.2	2.922
Mu	4.709	+37.6	+71.0	0	+66.5	+13.3	4.653
Theta	2.950	+203.0	+289.4	6	+256.6	+155.5	2.909
Zeta	2.824	+97.6	+168.6	3	+150.0	+81.1	2.798

All models were then optimized using VASP by allowing all structural parameters, including volume, cell shape, and atomic coordinates, to relax. The energies of the optimized structures can also be found in Table 2. Details of the optimized structures can be found in Tables S5–S13. After optimization, the rhombohedral model remains the lowest energy with the orthorhombic and cubic models coming in second and third lowest energy. The orthorhombic (γ) model optimized to a monoclinic unit cell, $a \neq b \neq c$ and only $\beta = 90°$, while the other two models retained their symmetry through the optimization. As the energies increase for the various optimized structures, the number of nearest neighbor Ga-Ga interactions increases and the corresponding Ga-Ga distances decrease. Table 2 lists the energies after optimization as well as the resulting nearest Ga-Ga distance showing the correlation between total energy and Ga-Ga interactions.

Calculations have shown that the rhombohedral model is the lowest energy both before and after optimization. This leads to the question of how does the rhombohedral structure arise from the "cubic" arranged starting point? The "cubic" starting point, for Ca_2Pt_3Ga, has a lattice parameter of 7.598 Å and a body diagonal distance of 13.160 Å. The primitive rhombohedral unit cell, within the face-centered cubic cell, has angles equal to 60° before optimization. After optimization these angles are 57.825° and 57.515° for Ca_2Pt_3Ga and Ca_2Pd_3Ga respectively. This collapsing of the angles, comprising the primitive unit cell, causes the expansion of the body diagonal. Optimization expands the lattice parameter by 1.43% to 7.708 Å. However, during optimization, the body diagonals do not expand congruently. Three body diagonals are congruent with a length of 13.627 Å while the fourth body diagonal shrinks to 12.482 Å. In the Pd case the three equivalent body diagonals are 13.754 Å while the fourth body diagonal shrinks to 12.412 Å. The shorter body diagonal is parallel to the direction that the Ga atoms are located in each of the four tetrahedra in the unit cell (see Figure 3). Calculated ICOHP values for the "cubic" starting point indicate that the Pt-Ga bonds (ICOHP = −1.857 eV) would become shorter as compared with the Pt-Pt bonds (ICOHP = −0.775 eV). These ICOHP values shed light on the driving force behind the corresponding distortion of the cubic unit cell to the rhombohedral structure by substituting Ga for Pd/Pt: shorter Pt-Ga contacts will contract one body-diagonal of the cubic cell.
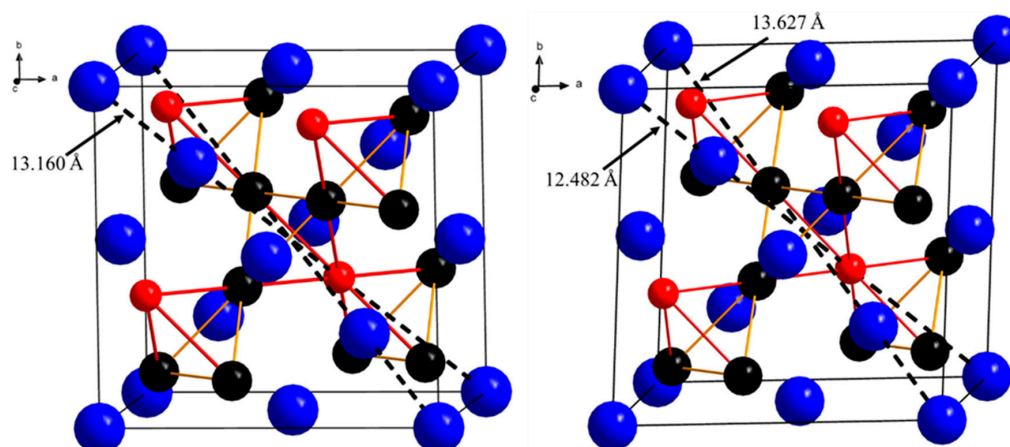

Figure 3. "Cubic" arranged starting point with 4 congruent body diagonals (**left**) optimized rhombohedral unit cell (**right**) with 3 body diagonals of 13.627 Å and 1 body diagonal of 12.482 Å. Red colored bonds shrink during optimization causing the reduction in body diagonal length from 011 to 100. Blue, black, and red atoms are Ca, Pt, and Ga respectively.

All "coloring" calculations performed above were evaluated for the case of $vec = 37e^-$/f.u. Models were also created for the Ca_2Pd_3Ge to determine if there were any differences by changing the vec to $38\ e^-$/f.u. The energies of the non-optimized and optimized colorings can be found in Table S4, and the results show the same trends as those for Ca_2M_3Ga (M = Pd, Pt): the lowest energy model shows rhombohedral coloring and the largest Ge-Ge nearest neighbor distance.

To shed light on the nature of the distortion of the cubic Laves phase structure of CaM_2 (M = Pd, Pt) upon the substitution of Ga for M and their stability, various total energies as well as the density of states (DOS) and crystal orbital Hamilton population (COHP) curves were determined for the binaries CaM_2 and ternaries Ca_2M_3Ga (M = Pd,Pt). With respect to the elemental solids, the binaries CaM_2 and ternaries Ca_2M_3Ga are favored. For the experimental structures, $CaPt_2$ has an especially high formation energy compared to $CaPd_2$; the experimental volume of $CaPt_2$ is ca. 10 $Å^3$/formula unit smaller than that of $CaPd_2$, although Pt is slightly larger than Pd (the 12-coordinate metallic radii are 1.39 (Pt) and 1.37 (Pd) [32]. This outcome may be an indication of relativistic effects on the valence orbitals of Pt, effects which can enhance empty *d*-filled *d* Ca-Pt *3d-5d* interactions as compared to Ca-Pd *3d-4d* interactions.

Total energy calculations for the "reactions" $2CaPt_2 + Ga \rightarrow Ca_2Pt_3Ga + Pt$ and $2CaPd_2 + Ga \rightarrow Ca_2Pd_3Ga + Pd$ illuminate significant aspects of the relative stability and formation of the ternaries. Both "reactions" yield favorable ΔE values, respectively, of -0.297 and -0.599 eV, and they can be separated into the sum of three hypothetical but revealing steps: (1) elemental substitution of Ga for M with no metric changes (volume, unit cell shape) in the cubic Laves phase structure; (2) volume change for the ternary without change in unit cell shape; and (3) distortion of the unit cell shape of the ternary at constant cell volume. Table 3 summarizes these results. The difference in overall total energies essentially arises from the energetic difference for step (1) between Pt and Pd cases: replacing Pt with Ga is energetically unfavorable whereas Pd for Ga is favorable. Since Ga (metallic radius of 1.50 Å [32]) is larger than either Pt or Pd, these energy differences reflect, in part, volume effects, but also are influenced by the relative Mulliken electronegativities [33], which increase Ga (3.2 eV) to Pd (4.45 eV) to Pt (5.6 eV). In the second step, both structures favorably expand by over 3% (based on unit cell volume) with slight energetic lowering. In the third step, both lattice distortions provide similar energetic stabilizations.

Table 3. Relative total energies (eV) for conversion of binary cubic Laves phases CaM_2 into ternary rhombohedral derivatives Ca_2M_3Ga (M = Pd, Pt). * = cubic unit cell metric with volume matching the corresponding binary compound; ** = cubic unit cell metric with volume matching the corresponding rhombohedral ternary compound. Specific total energies (eV/formula unit) for each component are listed in Supporting Information.

	2 CaPd$_2$	**+ Ga**	**$\rightarrow$**	**Ca$_2$Pd$_3$Ga**	**+ Pd**	**$\Delta E = -0.599$ eV**
(1)	2 CaPd$_2$	+ Ga	$\rightarrow$	Ca$_2$Pd$_3$Ga *	+ Pd	$\Delta E = -0.258$ eV
(2)	Ca$_2$Pd$_3$Ga *		$\rightarrow$	Ca$_2$Pd$_3$Ga **		$\Delta E = -0.042$ eV
(3)	Ca$_2$Pd$_3$Ga **		$\rightarrow$	Ca$_2$Pd$_3$Ga		$\Delta E = -0.299$ eV
	2 CaPt$_2$	**+ Ga**	**$\rightarrow$**	**Ca$_2$Pt$_3$Ga**	**+ Pt**	**$\Delta E = -0.297$ eV**
(1)	2 CaPt$_2$	+ Ga	$\rightarrow$	Ca$_2$Pt$_3$Ga *	+ Pt	$\Delta E = +0.115$ eV
(2)	Ca$_2$Pt$_3$Ga *		$\rightarrow$	Ca$_2$Pt$_3$Ga **		$\Delta E = -0.088$ eV
(3)	Ca$_2$Pt$_3$Ga **		$\rightarrow$	Ca$_2$Pt$_3$Ga		$\Delta E = -0.324$ eV

We now consider some specific aspects of the electronic structures of the binary CaM_2 and ternary Ca_2M_3Ga. The DOS and COHP for $CaPt_2$ are shown in Figure 4; the DOS shows a significant sharp peak at the Fermi level which suggests a potential electronic instability.
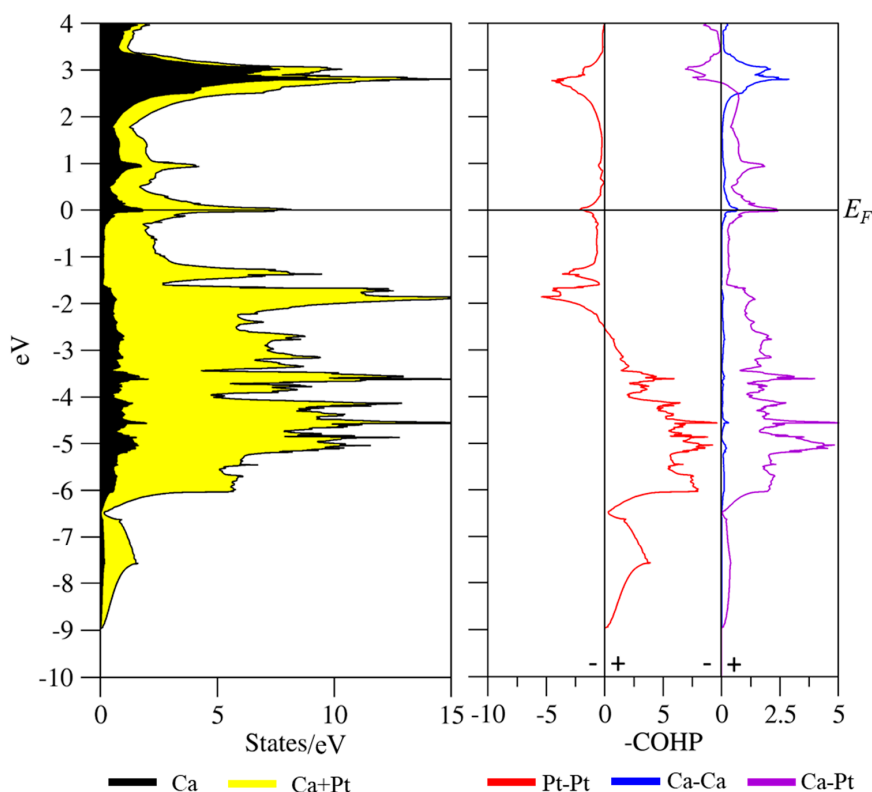
Figure 4. DOS (**left**) and -COHP (**right**) for CaPt$_2$ with $+/-$ indicating bonding/antibonding values of COHP curves. Ca-Ca and Ca-Pt interactions are magnified for comparison.

The precise reason for this peak and the possible instability has not been forthcoming to date and an electronic structure investigation was performed. Analysis of the band structure at the Fermi level, specifically at the W point, because there are bands with nearly zero slope near this point, shows that the Pt 5*d* atomic orbitals are major contributors to this peak. For each Pt atom the orbital contribution is split approximately as 80 percent 5*d* and 20 percent 6*p*, and the primary interatomic orbital interactions are 5*d*-5*d* π* interactions. Spin-orbit coupling was added to the Hamiltonian operator of CaPt$_2$ to see if the peak at the Fermi level would be affected. Figure S6 shows the DOS curve and band structure for these calculations. The degeneracies in the band structure at the high symmetry *k*-points are removed by the spin-orbit coupling; however, the peak at E_F is not affected. Furthermore, the application of spin-orbit coupling would only converge with a unit cell expanded by ~1.1 Å. A second hypothesis was to consider that vacancies might be playing a role to stabilize the structure. DOS calculations were subsequently performed using VASP on "Ca$_8$Pt$_{15}$" and "Ca$_8$Pt$_{12}$" models to see the effect of vacancies on the peak at E_F; these results can be seen in Figure S7. The peak is no longer present in the "Ca$_8$Pt$_{12}$" model only when all 4 vacancies are adjacent to each other so that the resulting defect Laves phase structure is missing an entire tetrahedron per unit cell. Lastly, DOS curves calculated for AEM$_2$ (AE = Ca, Sr, Ba; M = Ni, Pd, Pt), shown in Figure S8, indicate that as the size of the alkaline earth metal increases, the peak in the DOS moves away from E_F. These calculations have not identified the reason behind the potential electronic instability in CaM$_2$ and now the possibility of superconductivity is being investigated.

The Pt 5*d* band dominates the overall occupied DOS of CaPt$_2$ and the majority contribution to the overall polar covalent bonding via ICOHP values arises from Pt-Pt interactions, which switch from bonding to antibonding at an energy value corresponding to 12.42 e^-/formula unit. At the Fermi level, the Pt-Pt COHP curve shows a small antibonding peak, whereas the Ca-Pt and Ca-Ca COHPs show a small bonding peak. On transitioning to Ca$_2$Pt$_3$Ga, the peak at the Fermi level in the DOS of CaPt$_2$ has all but disappeared in the DOS curve of Ca$_2$Pt$_3$Ga (see Figure 5). There is a large range from ca.

−1.5 to +1 eV over which the DOS of Ca_2Pt_3Ga remains flat. The COHP curves have also changed in that the Pt-Pt interactions still transition to antibonding at −2.60 eV, although around the Fermi level they are mostly nonbonding rather than antibonding. Overall, at the Fermi level there are now no small peaks but mostly constant intensities of nonbonding or slightly bonding interactions with the Ca-Pt interactions still contributing the most to overall bonding.
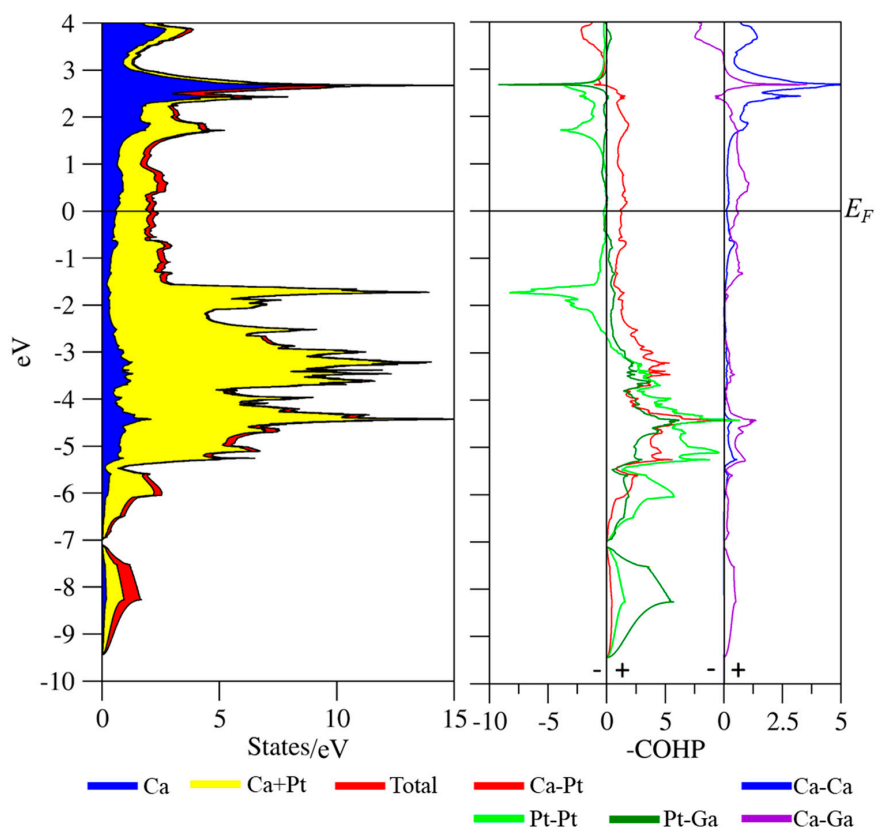

Figure 5. DOS (**left**) and COHP (**right**) for Ca_2Pt_3Ga with +/− indicating bonding/antibonding values of COHP curves. Ca-Ca and Ca-Ga interactions magnified for comparison.

The DOS and COHP curves for $CaPd_2$ (see Figure 6) and Ca_2Pd_3Ga (see Figure 7) look similar overall to those described above for the Pt counterparts, although there are a few distinct differences. The peak at the Fermi level in the DOS for $CaPd_2$ as well as the antibonding Pd-Pd peak in the COHP are not as intense nor as sharp as those observed for $CaPt_2$. The Pd-Pd interactions transition from bonding to antibonding at an energy which corresponds to 15.36 eV/formula unit. There is a similar minimum in the Pd 4*d* states at −1.40 eV which corresponds to 7.5 4*d* electrons/Pd. The DOS and COHP for Ca_2Pd_3Ga are similar to those for Ca_2Pt_3Ga. There is again a large energy range from ca. −1.8–1.8 eV over which the DOS remains flat.

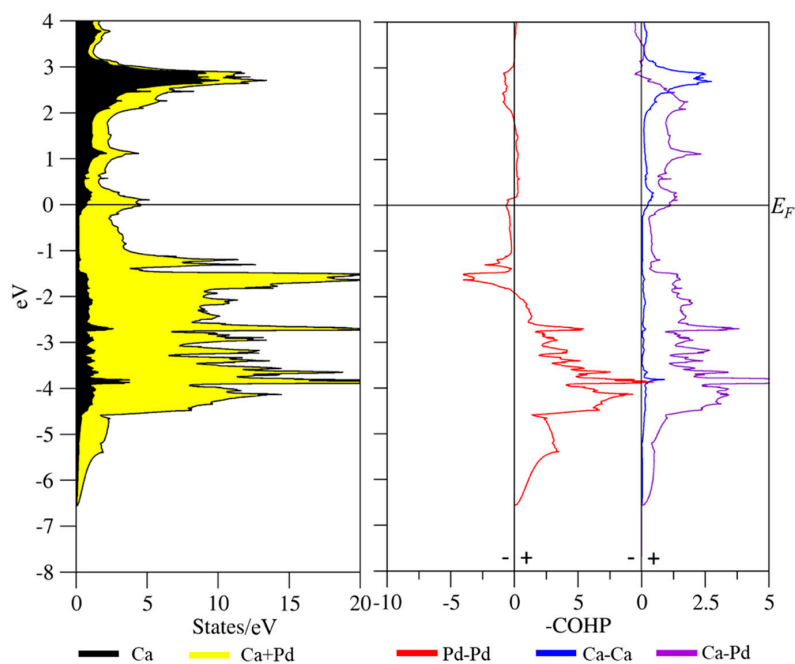**Figure 6.** DOS (**left**) and COHP (**right**) calculated for CaPd$_2$ with +/− indicating bonding/antibonding values of COHP curves. Ca-Pd and Ca-Ca interactions magnified for comparison.
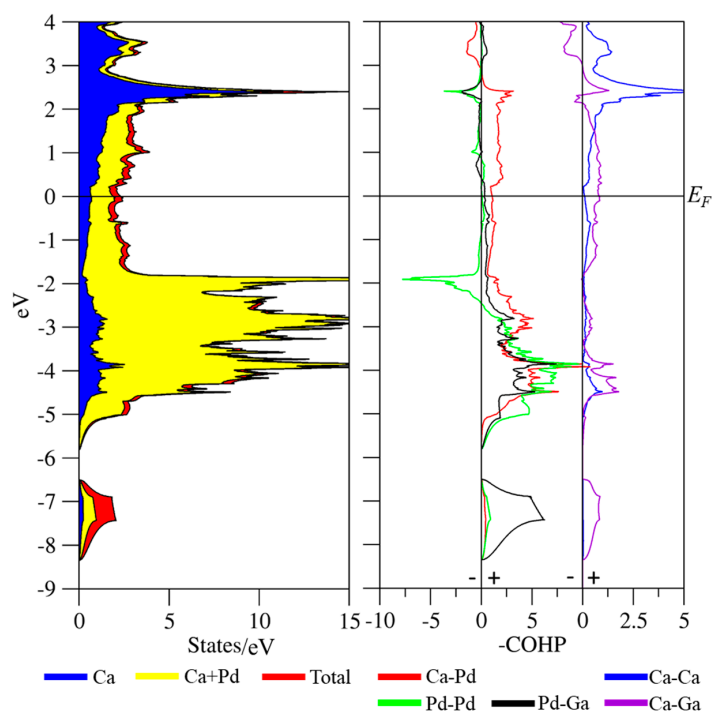

Figure 7. DOS (**left**) and COHP (**right**) calculated for Ca$_2$Pd$_3$Ga with +/− indicating bonding/antibonding values of COHP curves. Ca-Ca and Ca-Ga interactions magnified for comparison.

Tables S14–S17 contain the percent contributions of each type of interaction to the overall integrated COHP (ICOHP) values. These can be used as an indication to determine the bond energy contribution to the stability of a structure. The cubic binary Laves phases are dominated by the M-M (M = Pd, Pt) interactions at 62.95 and 58.41% for CaPt$_2$ and CaPd$_2$, respectively, whereas the Ca-Ca

interactions lend little to the overall ICOHP at only 1.47% and 2.12% for $CaPt_2$ and $CaPd_2$, respectively. The rest is made up by the Ca-M interactions. For the ternary compounds, there is a significant drop in the contributions from M-M interactions to the total polar-covalency because the majority of the total ICOHP comes from Ca-M and M-Ga interactions. In Ca_2Pt_3Ga, the Pt-Pt contribution is just 29.95%, and in Ca_2Pd_3Ga, the Pd-Pd contribution is 24.40%. The Ca-M and M-Ga interactions contribute ~30% each in both ternary compounds. Furthermore, in the ternary compounds, there are now Ca-Ga interactions that account for 5.81% and 7.89%, respectively, in Ca_2Pt_3Ga and Ca_2Pd_3Ga. The Ca-Ca bond populations continue to contribute less than 2.5% in all cases.

The analysis of the integrated Hamilton population curves to study the interatomic interactions is useful for mainly two-center interactions, and the use of crystal orbital overlap population (COOP) analysis has been applied to examine cubic vs. hexagonal Laves phases [34]. However, multi-center chemical bonding in Laves phases has also been described using an electron localizability indicator [35]. Laves phases AB_2 with a small electronegativity difference between the two components exhibit enhanced multi-center bonding because the effective charge transfer between A and B is small. However, if the electronegativity difference between A and B is large, the correspondingly greater effective charge transfer can lead to polyanions [35]. $CaPt_2$ and $CaPd_2$ are cases with a large electronegativity difference between the A and B atoms (3.2 eV for $CaPt_2$ and 2.25 eV for $CaPd_2$ [33]), but there most likely exists some multi-center bonding in these compounds, especially between the faces of the transition metal tetrahedra and the Ca atoms, bonding which would be affected by the substitution of one of the Pt or Pd atoms by Ga. The electronegativity difference between Ga and Ca is not as large (1.0 eV [33]), which creates less charge transfer between Ca and Ga and thereby shifts the valence electron density as compared to the binary structures. Electron localizability indicators were not evaluated during this study, but they would provide useful information regarding specifics of multi-center interactions in the ternary derivatives.

4. Conclusions

Two new fully ordered ternary gallium-containing Laves phase compounds, Ca_2Pt_3Ga and Ca_2Pd_3Ga, were synthesized and characterized by X-ray diffraction and electronic structure calculations. The compounds crystallize in a rhombohedrally distorted cubic $MgCu_2$-type structure. Ca_2Pd_3Ga was synthesized as a pure phase whereas Ca_2Pt_3Ga was only found co-existing with Ca_2Pt_2Ga and $CaPt_2$ and required the addition of small amounts of Ag to form. Total energy calculations performed on nine symmetrically inequivalent "coloring models" indicated that the rhombohedral coloring gave the lowest energy by 78.8 meV and 68.1 meV in the Pt and Pd cases respectively. ICOHP values from the "cubic" starting arrangement indicate that the M-Ga bonds tend to become shorter vs. M-M contacts. These shorter bonds cause a shrinking of the body diagonal from the corner of 011 to 100 which gives rise to the rhombohedrally distorted unit cell.

This computational study supports the group–subgroup relationship that R-3m is the highest maximal subgroup of Fd-3m and allows a fully ordered structure with the 3:1 ratio of M:Ga atoms. The rhombohedral coloring is the lowest energy way to color the "B" network in the Laves phase so that the Ga atoms avoid all homoatomic interactions and have the furthest nearest neighbor distance.

Author Contributions: A.T. performed the synthesis, characterization, and computational studies of all compounds, and wrote the first draft of the manuscript as part of his doctoral dissertation. G.J.M. managed the overall project and edited the final manuscript.

Conflicts of Interest: The authors declare no conflict of interest.

References

1. Jansen, M. Effects of relativistic motion of electrons on the chemistry of gold and platinum. *Solid State Sci.* **2005**, *7*, 1464–1474. [CrossRef]
2. Siggelkow, L.; Hlukhyy, V.; Faessler, T.F. The Influence of the Valence Electron Concentration on the Structural Variation of the Laves Phases $MgNi_{2-x}Ge_x$. *Z. Anorg. Allg. Chem.* **2017**, *643*, 1424–1430. [CrossRef]
3. Doverbratt, I.; Ponou, S.; Lidin, S. Ca_2Pd_3Ge, a new fully ordered ternary Laves phases structure. *J. Solid State Chem.* **2013**, *197*, 312–316. [CrossRef]
4. Stein, F.; Palm, M.; Sauthoff, G. Structure and stability of Laves phases. Part I—Critcal assessment of factors controlling Laves phase stability. *Intermetallics* **2004**, *12*, 713–720. [CrossRef]
5. Osters, O.; Nilges, T.; Schöneich, M.; Schmidt, P.; Rothballer, J.; Pielnhofer, F.; Weihrich, R. Cd_4Cu_7As, The First Representative of a Fully Ordered, Orthorhombically Distorted $MgCu_2$ Laves Phases. *Inorg. Chem.* **2012**, *51*, 8119–8127. [CrossRef] [PubMed]
6. Murtaza, A.; Yang, S.; Zhou, C.; Song, X. Influence of Tb on easy magnetization direction and magnetostriction of ferromagnetic Laves phase GdFe compounds. *Chin. Phys. B* **2016**, *25*, 096107. [CrossRef]
7. Manickam, K.; Grant, D.M.; Walker, G.S. Optimization of AB2 type alloy composition with superior hydrogen storage properties for stationary applications. *Int. J. Hydrogen Energy* **2015**, *40*, 16288–16293. [CrossRef]
8. Nash, C.P.; Boyden, F.M.; Whittig, L.D. Intermetallic compounds of alkali metals with platinum. A novel preparation of a colloidal platinum hydrogenation catalyst. *J. Am. Chem. Soc.* **1960**, *82*, 6203–6204. [CrossRef]
9. Xiao, C.; Wang, L.; Maligal-Ganesh, R.V.; Smetana, V.; Walen, H.; Thiel, P.A.; Miller, G.J.; Johnson, D.D.; Huang, W. Intermetallic $NaAu_2$ as a Heterogeneous Catalyst for Low-Temperature CO Oxidation. *J. Am. Chem. Soc.* **2013**, *135*, 9592–9595. [CrossRef] [PubMed]
10. Thimmaiah, S.; Miller, G.J. Influence of Valence Electron Concentration on Laves Phases: Structures and Phase Stability of Pseudo-Binary $MgZn_{2-x}Pd_x$. *Z. Anorg. Allg. Chem.* **2015**, *641*, 1486–1494. [CrossRef]
11. Seidel, S.; Janka, O.; Benndorf, C.; Mausolf, B.; Haarmann, F.; Eckert, H.; Heletta, L.; Pöttgen, R. Ternary rhombohedral Laves phases RE_2Rh_3Ga (RE = Y, La-Nd, Sm, Gd-Er). *Z. Naturforsch.* **2017**, *72*, 289–303. [CrossRef]
12. Dwight, A.E.; Kimball, C.W. A rhombohedral Laves phase. Terbium-ron ($TbFe_2$). *Acta Cryst. Sect. B* **1974**, *30*, 2791–2793. [CrossRef]
13. Burdett, J.K.; Canadell, E.; Hughbanks, T. Symmetry control of the coloring problem: The electronic structure of MB2C2 (M = calcium, lanthanum, . . .). *J. Am. Chem. Soc.* **1986**, *108*, 3971–3976. [CrossRef]
14. Jepsen, O.; Andersen, O.K. *TB-LMTO*, version 47; Max-Planck-Institut für Festkörperforshcung: Stuttgart, Germany, 2000.
15. Von Barth, U.; Hedin, L. Local exchange-correlation potential for the spin-polarized case. *J. Phys. C* **1972**, *5*, 1629. [CrossRef]
16. Koelling, D.D.; Harmon, B.N. A technique for relative spin-polarized calculations. *J. Phys. C* **1977**, *10*, 3107–3114. [CrossRef]
17. Kresse, G.; Hafner, J. Ab initio molecular dynamics for liquid metals. *Phys. Rev. B* **1993**, *47*, 558. [CrossRef]
18. Kreese, G.; Furthmüller, J. Efficient iterative schemes for ab initio total-energy calculations using a plane-wave basis set. *Phys. Rev. B* **1996**, *54*, 11169–11186. [CrossRef]
19. Blöchl, P.E. Projector augmented-wave method. *Phys. Rev. B* **1994**, *50*, 17953–17979. [CrossRef]
20. Perdew, J.P.; Burke, K.; Wang, Y. Gerneralized gradient approximation for the exchange-correlation hole of a many-electron system. *Phys. Rev. B* **1996**, *54*, 16533–16539. [CrossRef]
21. Monkhorst, H.J.; Pack, J.D. Special points for Brillouin-zone integrations. *Phys. Rev. B* **1976**, *13*, 5188. [CrossRef]
22. Blöchl, P.E.; Jepsen, O.; Andersen, O.K. Improved tetrahedron method for Brillouin-zone integrations. *Phys. Rev. B* **1994**, *49*, 16223–16233. [CrossRef]
23. *PowderCell*, version 2.3; Federal Institute for Materials Research and Testing: Berlin, Germany, 2000.
24. *APEX-II*; Bruker AXS Inc.: Madison, WI, USA, 2013.
25. *SAINT-V8.27*; Bruker AXS Inc.: Madison, WI, USA, 2013.
26. *SHELXTL-v2008/4*; Bruker AXS Inc.: Madison, WI, USA, 2013.

27. Brandenburg, K. *Diamond*, version 3.2; Crystal Impact GbR: Bonn, Germany, 2011.

28. Petricek, V.; Dusek, M.; Palatinus, L. *Structure Determination Software Programs*; Institute of Physics: Praha, Czech Republic, 2006.

29. Cenzual, K.; Chabot, B.; Parthe, E. Yttrium rhodium germanide (Y_2Rh_3Ge), a rhombohedral substitution variant of the $MgCu_2$ type. *J. Solid State Chem.* **1987**, *70*, 229–234. [CrossRef]

30. Burdett, J.K.; McLarnan, T.J. Geometrical and electronic links among the structures of MX2 solids: Structural enumeration and electronic stability of pyritelike systems. *Inorg. Chem.* **1982**, *21*, 1119–1128. [CrossRef]

31. Xie, W.; Miller, G.J. β-Mn-Type $Co_{8+x}Zn_{12-x}$ as a Defect Cubic Laves Phase: Site Preferences, Magnetism, and Electronic Structure. *Inorg. Chem.* **2013**, *52*, 9399–9408. [CrossRef] [PubMed]

32. Wells, A.F. *Structural Inorganic Chemistry*, 5th ed.; Clarendon Press: Oxford, UK, 1984.

33. Pearson, R.G. Absolute Electronegativity and Hardness: Application to Inorganic Chemistry. *Inorg. Chem.* **1988**, *27*, 734–740. [CrossRef]

34. Johnston, R.; Hoffmann, R. Structure-Bonding Relationships in the Laves Phases. *Z. Anorg. Allg. Chem.* **1992**, *616*, 105–120. [CrossRef]

35. Ormeci, A.; Simon, A.; Grin, Y. Structural Topology and Chemical Bonding in Laves Phases. *Angew. Chem.* **2010**, *49*, 8997–9001. [CrossRef] [PubMed]